

DNS of a Spatially Developing Turbulent Mixing Layer from Co-flowing Laminar Boundary Layers

Juan D. Colmenares F.¹ and Svetlana V. Poroseva²
The University of New Mexico, Albuquerque, NM 87131

Yulia T. Peet³
Arizona State University, Tempe, AZ 85287

and

Scott M. Murman⁴
NASA Ames Research Center, Moffett Field, CA 94035

Understanding the development of a turbulent mixing layer is essential for various aerospace applications. In particular, experiments found that the flow development is highly sensitive to inflow conditions, which are difficult to reproduce in the flow simulations. In previous direct numerical simulations (DNS) of temporarily and spatially developing turbulent mixing layers, idealized inflow conditions based on mathematical approximations of the mean velocity profile were used to facilitate turbulent flow conditions. The current paper presents results of DNS of a spatially developing turbulent mixing layer, where co-flowing laminar boundary layers over a splitter plate are used as inflow conditions; no artificial perturbations are seeded into the flow. The goal is to closer replicate a naturally developing mixing layer. The flow conditions used in simulations closely match those in experiments by Bell & Mehta (1990). DNS were conducted using the spectral-element code Nek5000. Effects of the splitter plate thickness and the computational domain size in the spanwise direction on the flow development are analyzed. Profiles of the mean flow velocity and the Reynolds stresses are compared with the experimental data.

Nomenclature

A	=	Aspect ratio between the spanwise domain length and the momentum thickness, L_z/θ
h	=	thickness of the splitter plate at the trailing edge
K_x, K_y, K_z	=	normal Reynolds stresses integrated across the mixing layer
L_x, L_y, L_z	=	computational domain sizes in streamwise, transverse, and spanwise directions
N	=	polynomial order of the Lagrange interpolants
p	=	pressure
Re_δ	=	Reynolds number with respect to the boundary layer thickness, $U_\infty \delta_{99}/\nu$
U, V, W	=	streamwise, transverse, and spanwise components of the instantaneous flow velocity
U_∞	=	free-stream velocity
U_1, U_2	=	free-stream velocity of high- and low-speed streams, respectively
U_c	=	centerline velocity, $0.5(U_1 + U_2)$

¹ Graduate Student, Mechanical Engineering, MSC01 1104, 1 UNM Albuquerque, NM 87131-00011, AIAA Student Member.

² Associate Professor, Mechanical Engineering, MSC01 1104, 1 UNM Albuquerque, NM 87131-00011, AIAA Associate Fellow.

³ Assistant Professor, Aerospace Engineering & Mechanical Engineering, Arizona State University, 501 E. Tyler Mall, Tempe, AZ 85287-6106, AIAA Member.

⁴ Aerospace Engineer, NASA Ames Research Center, Moffett Field, CA 94035.

u, v, w	=	turbulent velocity fluctuations in streamwise, transverse, and spanwise directions
x, y, z	=	streamwise, transverse, and spanwise direction coordinates
y_0	=	mixing layer centerline
δ_{99}	=	boundary layer thickness
δ_{ML}	=	mixing layer thickness
δ_ω	=	mixing layer vorticity thickness, $\Delta U / (\partial \langle U \rangle / \partial y)$
ΔU	=	velocity difference, $U_1 - U_2$
\mathbf{u}, \mathbf{v}	=	instantaneous velocity vectors
∇	=	gradient operator
η	=	normalized transverse coordinate, $(y - y_0) / \delta_{ML}$
η_K	=	Kolmogorov length scale
θ	=	momentum thickness
ν	=	kinematic viscosity
τ_f	=	flow-through time, L_x / U_c
$\langle \dots \rangle_{en}$	=	ensemble average
$\langle \dots \rangle$	=	ensemble and spanwise average
$\langle \dots \rangle_V$	=	volume average
$\langle \dots \rangle_T$	=	time and volume average

I. Introduction

Planar mixing layers occur when two parallel streams with different velocities, initially separated by a splitting surface, come into contact and generate a shear layer at the interface due to momentum transfer. This flow configuration appears in many aerospace applications such as, for example, flow reactors and combustion chambers, where the rate of combustion is governed by turbulent mixing in the shear layer¹, and at the nozzle of turbine engines of commercial aircraft, where a level of noise generated by a turbine is proportional to the turbulent kinetic energy in the shear layer caused by the jet of exhaust gases². Because of their crucial role, turbulent mixing layers have been studied for more than a half of century, experimentally and numerically.

A review of experimental data sets³ revealed a discrepancy among experimental results taken at similar free-stream conditions, and concluded that this was mostly due to inconsistencies between the inflow conditions used in the considered experiments. Further studies^{3,4,6} confirmed that the mixing layer structure far downstream a splitter plate was closely related to the inflow conditions. A particular role of the boundary layer parameters developed on the high-speed stream side of the splitter plate on the flow transition and the flow self-similarity was demonstrated in Ref. 5. Dependence of the flow structure on the splitter plate geometry⁷, velocity ratio between high- and low-speed free streams^{8,9}, and free-stream turbulence intensity¹⁰ was also observed in experiments. However, a detailed analysis of experimental data is complicated by the fact that different experiments studied the mixing layer structure under different flow conditions.

Numerical simulations can in principle compensate for this gap in knowledge. Previously, temporarily¹¹⁻¹³ and spatially developing planar mixing layers¹⁴⁻¹⁹ were simulated in particular using large eddy simulations (LES) and direct numerical simulations (DNS). LES have been used to study the large-scale motion of the flow, analyzing the effects of inflow conditions on the evolution of the mixing layer¹⁷ and that of the computational domain spanwise dimension on the mixing layer growth rate^{11,16}. DNS have been conducted to provide a comprehensive description of mixing layers in transition and fully-turbulent regimes¹²⁻¹⁵, also to characterize small-scale turbulent structures through coherent fine-scale eddies visualization¹⁴ and the structure-function scaling¹⁵.

Most previous DNS used modeled inflow conditions to facilitate turbulence in a mixing layer and assumed an infinitely thin splitter plate. Whereas these steps help to reduce the cost of computations, they are not representative of inflow conditions used in the experiments and may lead to unphysical flow solutions. In Refs. 18 and 19, DNS of a mixing layer generated by co-flowing laminar boundary layers developed over a splitter plate were conducted, with various effects of the splitter plate geometry on the flow development being analyzed.

Laminar boundary layers occur as inflow conditions in a naturally developing mixing layer and some applications. They were also used in experiments^{6,7} and are easier to reproduce in simulations. However, simulations with such inflow conditions are more demanding on computational resources. As a result, previous DNS^{18,19} with the laminar boundary layers as the inflow conditions for a mixing layer were conducted at much lower Reynolds numbers than those attained in the experiments.

The goal of the current study is to understand requirements on the computational domain dimensions for achieving spatially-developing turbulent mixing within the domain when using laminar boundary layers over a splitter plate as inflow conditions at the Reynolds numbers matching experimental values⁶ without imposing artificial perturbations on the flow to trigger the flow transition. Particular attention is given to the analysis of the effects of the splitter plate thickness and the spanwise length of the computational domain on the mixing layer development.

The paper begins with a review of the DNS methodology and the computational setup of the mixing layer case used in the study. In the Results section, the flow conditions at different locations in the streamwise directions are discussed, profiles of the mean velocity and the Reynolds stresses are provided and compared against experimental data⁶. The mixing layer thickness growth and the turbulent kinetic energy integrated across the mixing layer are plotted as functions of the streamwise location to illustrate the influence of the splitter plate thickness and the domain spanwise length on the flow development. Large- and small-scale vortex structures present in the flow are visualized using the objective vortex-identification technique²⁰ to further illustrate dynamics of the simulated flow. Adequacy of the chosen domain dimensions in the streamwise and transverse directions is also discussed.

II. DNS methodology

In the current study, governing equations are solved using a spectral-element method (SEM)²¹, implemented in the code Nek5000²². This method combines the geometrical flexibility of finite element methods with the accuracy of spectral methods. The non-dimensional incompressible Navier-Stokes equations

$$\begin{aligned} \frac{\partial}{\partial t} \mathbf{u} + (\mathbf{u} \cdot \nabla \mathbf{u}) &= -\nabla p + \nabla^2 \mathbf{u} / \text{Re} \quad \text{in } \Omega, \\ \nabla \cdot \mathbf{u} &= 0 \quad \text{in } \Omega, \end{aligned} \quad (1)$$

are solved in their weak formulation:

$$\begin{aligned} \frac{\partial}{\partial t} (\mathbf{u}, \mathbf{v}) + (\nabla \mathbf{u}, \nabla \mathbf{v}) / \text{Re} + (\mathbf{u} \cdot \nabla \mathbf{u}, \mathbf{v}) &= (p, \nabla \cdot \mathbf{v}), \quad \forall \mathbf{v} \in X, \\ -(q, \nabla \cdot \mathbf{u}) &= 0, \quad \forall q \in Y, \end{aligned} \quad (2)$$

where Ω is the domain of the numerical solution. The problem in Eq. (2) can be defined as finding $\mathbf{u} \in X$ and $p \in Y$ such that Eq. (2) is satisfied, where the inner product in the equation, (\cdot, \cdot) , is

$$(\phi, \psi) \equiv \int_{\Omega} \phi(x) \psi(x) dx. \quad (3)$$

The X and Y in Eq. (2) are proper subspaces for \mathbf{u}, \mathbf{v} and p, q defined as:

$$\begin{aligned} X &= \{\mathbf{v}: v_i \in H^1(\Omega), i = 1, \dots, d\} \\ Y &= \mathcal{L}^2(\Omega). \end{aligned} \quad (4)$$

In Eq. (4), $\mathcal{L}^2(\Omega)$ is a space of functions that are square integrable in the domain Ω , meaning if $\phi \in \mathcal{L}^2(\Omega)$, then $\int_{\Omega} \phi^2 dx < \infty$. The space $H^1(\Omega)$ consists of functions that are in $\mathcal{L}^2(\Omega)$ and which first derivatives are also in $\mathcal{L}^2(\Omega)$.

Equation (2) is discretized in space by the Galerkin approximation²³, where the discrete analogues of the spaces X and Y are chosen in the tensor product space of N th-order Lagrange polynomial interpolants, $h_i^N(x)$, defined on Gauss-Lobatto-Legendre (GLL) quadrature points, following the $\mathbb{P}_N - \mathbb{P}_N$ formulation in Ref. 24. The polynomial interpolants satisfy $h_i^N(\xi_j^N) = \delta_{ij}$, where $\xi_j^N \in [-1, 1]$ denotes the location in elemental (local) coordinates of a GLL quadrature point with the index j and δ_{ij} is the Kronecker delta.

Inside every element, there are $(N + 1)^d$ GLL quadrature points, also called collocation points, where the exponent d is the number of dimensions of the problem. For an element in \mathbb{R}^3 , the numerical solution, u , and its derivatives are expressed in terms of the interpolating functions:

$$u(x, y, z, t) = \sum_{i=0}^N \sum_{j=0}^N \sum_{k=0}^N u_{ijk}(t) h_i^N(x) h_j^N(y) h_k^N(z) \quad (5)$$

$$\partial u(x, y, z, t) / \partial x = \sum_{i=0}^N \sum_{j=0}^N \sum_{k=0}^N u_{ijk}(t) (2/|J|) [h_i^N(x)]' h_j^N(y) h_k^N(z) \quad (6)$$

where $|J|$ is the determinant of the Jacobian matrix that relates global and local coordinate systems, etc. It should be noted that the velocity and pressure fields, which are represented as in Eq. (5), are $C^0(\Omega)$ continuous, while their derivatives (Eq. (6)) are discontinuous at the elemental interfaces.

Discretization in time is done using the high-order splitting method²⁵, which uses different treatment for linear and non-linear terms. The non-linear part of Eq. (2) is treated explicitly by the third-order extrapolation (EXT3), while viscous terms are treated implicitly by the third-order backward difference scheme (BDF3). Because of the explicit part in the time-stepping procedure, the Courant-Friedrichs-Levy (CFL) number must satisfy the condition $CFL = |\mathbf{u}| \Delta t / \Delta x < 0.5$ throughout the domain, where Δt is the size of the time-step and Δx is the grid spacing based on GLL quadrature points.

Special care is taken to eliminate aliasing errors from the non-linear terms²³, which occur due to inexact quadrature of higher-order polynomials that represent these terms. In this study, over-integration is used as a de-aliasing procedure, where the non-linear terms are integrated exactly by computing them on a fine grid, which contains $3(N + 1)/2$ Gauss-Legendre (GL) quadrature points. The number of GL points is then sufficient for the exact Gauss quadrature of the terms.

III. Computational setup

Flow conditions used in DNS were chosen to closely match those in experiments⁶. In the experiments, two cases with both laminar and turbulent boundary layers developed on a splitter plate used as inflow conditions for a mixing layer were investigated. Only the case with the laminar boundary layers is reproduced in our simulations. The laminar boundary layer parameters from the experiments are $U_1 = 15 \text{ m/s}$ and $U_2 = 9 \text{ m/s}$ for the free-stream velocities on the high-speed and low-speed sides respectively, with boundary layer thicknesses of $\delta_1 = 0.40 \text{ cm}$ and $\delta_2 = 0.44 \text{ cm}$. Non-dimensional flow parameters are provided in the table below:

Table 1. Laminar boundary layer parameters at the splitter plate trailing edge from experiments⁶.

Condition	U_∞ / U_1	δ_{99} / δ_1	θ / δ_1	Re_δ
High-speed side	1.0	1.0	0.13	3974
Low-speed side	0.6	1.1	0.15	2623

Flow parameters with index 1 correspond to those in the boundary layer developed on the high-speed stream side of the splitter plate.

Experimental data for velocity profiles in the laminar boundary layers are not available. Therefore, emphasis was placed to closely match in simulations the boundary layer thickness and the momentum thickness of the boundary layer formed on the high-speed stream side of the splitter plate (see Table 1). This is due to a peculiar role that this boundary layer plays on the flow transition and the flow self-similarity found by experiments⁵.

Free-stream turbulence conditions from experiments are difficult to match in simulations. However, experimental studies¹⁰ have shown that the plane mixing layer development is not affected by velocity fluctuations as long as they have an intensity of less than 0.6%. In Ref. 6, this level was $\sim 0.15\%$ in the streamwise fluctuations and $\sim 0.5\%$ in the other directions. Therefore, no free-stream turbulence condition was used in simulations.

In order to analyze the effects of the splitter plate thickness and the computational domain spanwise dimension on the mixing layer development, simulations were conducted in three different flow geometries.

Case 1 (baseline case), has dimensions $x/\delta_1 = [-170, 170]$ in the streamwise direction, where $x = 0$ is at the trailing edge of the splitter plate and $x > 0$ is the mixing region. The total domain length is $L_x/\delta_1 = 340$, while the mixing layer region is $L_x^{(ML)}/\delta_1 = 170$. The splitter plate is located in the region $x/\delta_1 = [-160, 0]$ on the high-speed side. A short development region was added upstream of the splitter plate, at $x/\delta_1 = [-170, -160]$, where the symmetry condition was applied at the lower boundary to avoid the singularity of solutions that would otherwise occur at the leading edge of the flat plate. On the low-speed side, the plate extends in $x/\delta_1 = [-76, 0]$, with the region in $x/\delta_1 < -76$ at $y < 0$ being outside of the computational domain. The length of the splitter plate was selected so that the boundary layers developing on the both sides of the splitter plate would achieve the boundary layer thicknesses

close to the experimental values, shown in Table 1. The length of the mixing layer region was selected to allow transition to full turbulence within the computational domain, based on the semi-empirical analysis^{5,26} and the local Reynolds number from experimental results obtained under similar flow conditions⁵. According to a review of different studies on planar mixing layers²⁶, a minimum local Reynolds number $Re = \delta_{ML}\Delta U/\nu \sim 2 \times 10^3$ is required to trigger transition to turbulence. This has been achieved in our simulations within the chosen computational domain.

In the transverse direction (y), the domain extends in $y/\delta_1 = [-35, 35]$. The splitter plate is assumed to be infinitely thin in this case, and it is located at $y = 0$. The transverse dimension of the domain, $L_y/\delta_1 = 70$, is approximately eight times larger than the maximum value of the mixing layer vorticity thickness δ_ω defined as

$$\delta_\omega = \Delta U / (\partial \langle U \rangle / \partial y)_{\max} \quad (7)$$

The mean velocity $\langle U \rangle$ is defined as an ensemble and a spanwise-averaged quantity at each streamwise and vertical location. The value $\delta_{\omega, \max}/\delta_1 \approx 8.7$ was estimated based on experimental data⁶ and the current domain size in the streamwise direction. This domain length was assumed to be sufficient for the study, as previous DNS^{14,15} of a mixing layer showed the lack of the result sensitivity to this parameter when it varied in the interval of $6.96 < L_y/\delta_{\omega, \max} < 8.3$.

Figure 1 shows the domain profile in the streamwise ($x/\delta_1 = [-170, 170]$) and transverse directions used in Case 1. In the spanwise direction, the domain in this case extends in $z/\delta_1 = [0, 23.4]$. This was considered large enough to have negligible effect on the mixing layer growth rate based on the aspect ratio¹⁶ $A = L_z/\theta_{\max} > 10$, where θ_{\max} is the maximum mixing layer momentum thickness expected to occur within the domain based on the experimental data⁶. Here, the mixing layer momentum thickness is defined as in Ref. 16:

$$\theta = (1/\Delta U^2) \int_{-\infty}^{\infty} (U_1 - \langle U \rangle)(\langle U \rangle - U_2) dy. \quad (8)$$

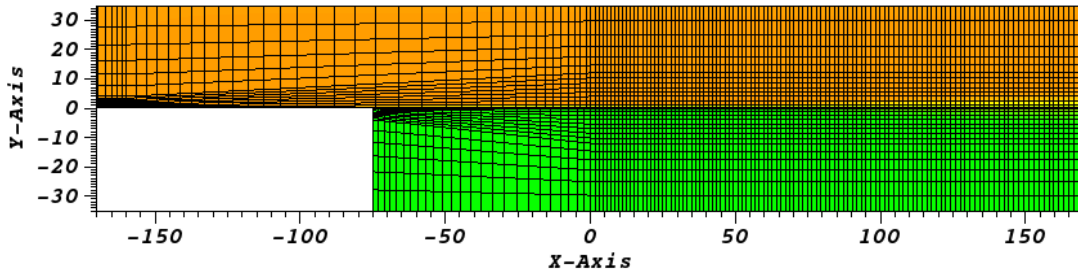


Figure 1. Mesh elements shown without internal collocation points. Orange: high-speed stream, green: low-speed stream.

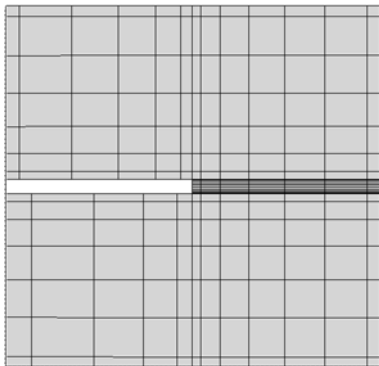


Figure 2. Grid elements with internal quadrature points near the trailing edge of the splitter plate (white color), shown between $x/\delta_1 = [-0.8, 0.8]$ and $y/\delta_1 = [-0.8, 0.8]$.

Case 2 (thick plate) simulated in our study has the same domain dimensions in the three directions as Case 1, but the splitter plate has the finite uniform thickness of $h/\delta_1 \sim 0.0625$, which is equal to the trailing edge thickness of the splitter plate used in the experiments⁶. Additional elements of the same thickness as the plate are added downstream the thick plate to maintain a conforming grid required by the solver. The grid around the trailing edge of the thick splitter plate is shown in Fig. 2.

In **Case 3** (large domain), the domain dimensions in the streamwise and transverse directions were the same as in Cases 1 and 2, but the spanwise dimension was twice as large: $z/\delta_1 = [-23.4, +23.4]$. The splitter plate was infinitely thin as in Case 1.

Polynomials of order of $N = 11$ were used as basis functions for the numerical method in all cases, which is typical in DNS using SEM^{27,28}. In the boundary layer region, spectral elements were clustered near the walls of the splitter plate in order to accurately resolve the laminar boundary layers. In a preliminary study, it was found that approximately one (1) spectral element across the boundary

layer thickness is enough to resolve the laminar boundary layer. A size of the spectral elements near the wall was adjusted to approximately match the size of the boundary layer thickness, δ_{99} , as a function of the streamwise location. Elements were clustered near the trailing edge of the splitter plate to accurately capture flow in this section.

In the mixing layer region, elements were clustered near the flow centerline ($y = 0$), where elements have a size of $\Delta y^e = 1.17\delta_1$. In the grid, the element size grows from the centerline towards the boundaries of the domain ($y/\delta_1 = -35$ and $y/\delta_1 = 35$) at the growth rate of $r = 1.05$ inside the inner region, which corresponds to $|y/\delta_1| < 10$, and $r = 1.2$ outside of this region ($10 < |y/\delta_1| < 35$). Here, $r = \Delta y^{i+1}/\Delta y^i$ is the ratio between the sizes of adjacent elements Δy^{i+1} and Δy^i , where the element of size Δy^{i+1} is located farther from the centerline than the element of size Δy^i .

In the streamwise and spanwise directions, a size of $\Delta x^e = \Delta z^e = 1.17\delta_1$ was used. The current grid was designed to satisfy the requirement of $(\delta x \cdot \delta y \cdot \delta z)^{1/3} < 4\eta_K \div 8\eta_K$, where $\delta x, \delta y, \delta z$ is the largest spacing between quadrature points in streamwise, transverse and spanwise directions, and η_K is the Kolmogorov length scale given by $\eta_K = (\nu^3/\varepsilon)^{1/4}$, with ν being kinematic viscosity and ε being the viscous dissipation rate of turbulent kinetic energy. This is comparable to the grid resolution used in previous DNS with spectral methods^{27,28}.

The grids used in Cases 1 and 2 contained a total of 140-160 million collocation (quadrature) points, while Case 3 had ~280 million collocation points.

Boundary conditions were only applied to the velocity field. The boundary conditions for pressure were computed automatically by the code to ensure that the continuity equation was satisfied^{22,29}. Fixed uniform velocity profile was set at the inlet, which was located at $x/\delta_1 = -170$ for the high-speed stream and at $x/\delta_1 = -75$ for the low-speed stream, given by:

$$U(x = x_i, y, z, t) = \begin{cases} U_1 & \text{if } y > 0 \\ U_2 & \text{if } y < 0 \end{cases}; \quad V(x = x_i, y, z, t) = W(x = x_i, y, z, t) = 0. \quad (9)$$

No-slip boundary condition was applied on the splitter plate. Outflow condition, $[PI + \nabla \mathbf{u}] \cdot \hat{\mathbf{n}} = 0$, was applied at the outlet ($x_o = 170$), where I is the identity matrix, and $\hat{\mathbf{n}}$ is the unit vector normal to the boundary. Outflow condition was also applied at the lower boundary ($y/\delta_1 = -35$). An initial attempt was made to use outflow boundary condition on both the upper and lower sides of the domain, but this resulted in an ill-posed problem since boundary conditions for the velocity field were under-determined. To avoid this, the ‘‘outflow-normal’’ condition were applied at the upper boundary ($y/\delta_1 = 35$), where the velocity component normal to the boundary was set free ($\partial V/\partial n = 0$) and the tangent velocity components were fixed ($U = U_1, W = 0$). In the spanwise direction, periodic boundary conditions were applied.

For the flow analysis, statistics were collected when the flow became statistically stationary. Duration of the initial transient period, not used in the data collection, was approximately 2.4 flow-through times $\tau_f = L_x/U_c$, or a simulation time of $t = 500$ normalized by δ_1/U_1 . The duration of the initial transient was determined by examining the evolution of the volume-averaged contributions to the flow kinetic energy from streamwise, $\langle U^2 \rangle_V$, transverse, $\langle V^2 \rangle_V$, and spanwise, $\langle W^2 \rangle_V$, components of instantaneous velocity (Figures 3a, 3c, and 3e). In the figure, all velocities are normalized by the high-speed free-stream velocity U_1 . Figures 3b, 3d, and 3f show the running time averages of the volume-averaged quantities, at $t > 500$. The Case 1 and Case 2 simulations run up to time $t = 2300$ (approximately $10.9 \tau_f$). Case 3 was terminated at $t = 1400$ due to several reasons discussed in the *Results* section.

Ensemble-averaged statistics were calculated in a post-processing computation as following

$$\langle Q \rangle_{en}(x, y, z) = \frac{1}{N_s} \sum_{i=1}^{N_s} Q_i(x, y, z), \quad (10)$$

where Q is the quantity to be averaged and N_s is the number of flow realizations or ‘‘snapshots’’. After that, the data were also averaged in the spanwise direction:

$$\langle Q \rangle(x, y) = \frac{1}{L_z} \int_0^{L_z} \langle Q \rangle_{en}(x, y, z) dz. \quad (11)$$

This step utilizes the flow homogeneity in the spanwise direction to improve the quality of collected statistics. Integration is done using the Gaussian quadrature over the Gauss-Lobatto-Legendre quadrature points.

A total of 504 snapshots were taken over a duration of $\sim 8.5 \tau_f$, or simulation time $t = 1800$, for simulations in Cases 1 and 2. Flow realizations in Case 3 were collected over a half of that time: $t = 900$.

The most of the simulations were conducted on the Pleiades supercomputer at the NASA High-End Computing Capability (HECC) using Ivy Bridge processor nodes (10-core Intel Xeon E5-2680v2, 2.8 GHz).

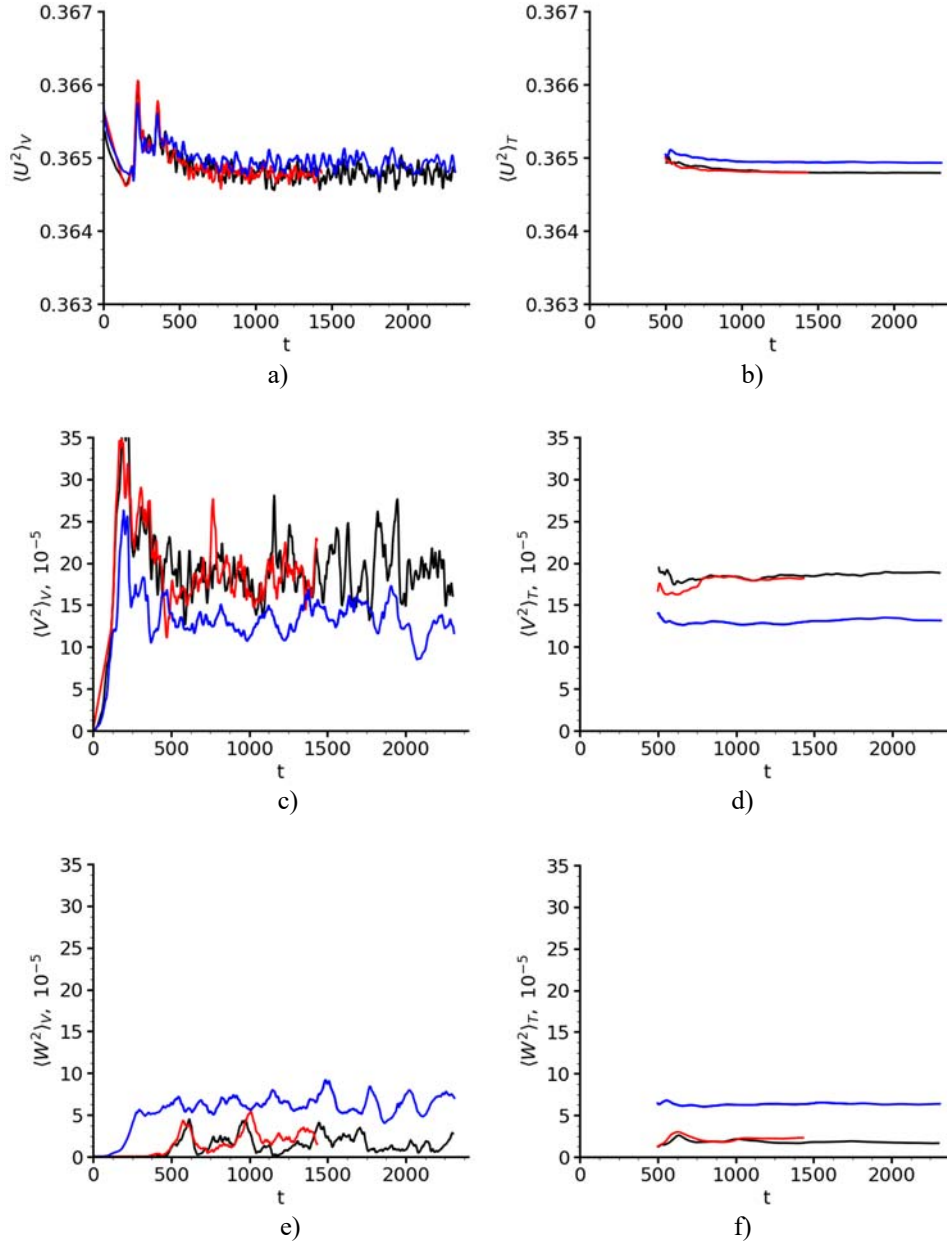


Figure 3. Evolution of contributions to the flow kinetic energy from: a,c,d) volume-averaged instantaneous velocities and b,d,e) volume-averaged instantaneous velocities averaged from time $t=500$ to the current time. Color scheme: black – Case 1, blue – Case 2, red – Case 3.

IV. Results

As the first step, we analyze characteristics of the simulated boundary layers at the trailing edge of the splitter plate. In figure 4, the mean velocity profiles from DNS are compared with the Blasius solution³¹. No experimental data are available for this flow parameter to compare with. In the figure, velocities are normalized with respect to U_1 ,

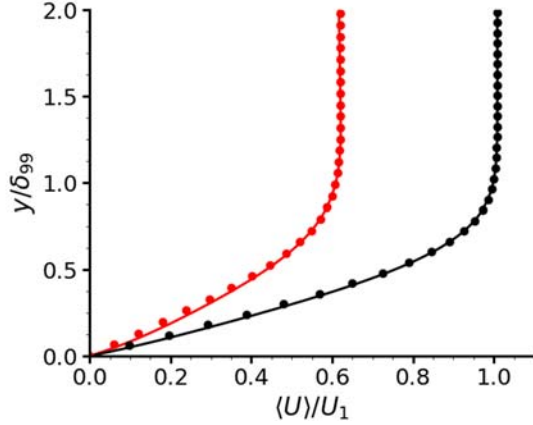


Figure 4. Mean velocity profiles of boundary layers at the trailing edge of the splitter plate, on the high-speed (black) and low-speed (red) sides. Notation: circles – the Blasius solution³¹, lines – DNS results.

$Re_\omega = \delta_\omega \Delta U / \nu \approx 10,887$, where δ_ω is calculated here as $\delta_\omega \approx \sqrt{\pi} \delta_{ML}$. The mixing layer thickness, δ_{ML} , is determined by computing the least-squares fit of the mean velocity profile to the error function profile shape:

$$\langle U \rangle \approx [1 + \text{erf}(\eta)]/2, \quad (12)$$

$$\eta = (y - y_0) / \delta_{ML}, \quad (13)$$

In (13), y_0 is the centerline of the mixing layer. Both parameters, y_0 and δ_{ML} were computed using the *curve_fit* function from the *scipy.optimize* library³⁰, available for Python 2.7 programming language.

The normalized mean velocity profiles, $(\langle U \rangle - U_2) / \Delta U$, are shown at different streamwise locations far downstream the splitter plate ($x / \delta_1 > 100$) in Fig. 5. As seen in the figure, all profiles collapse in this flow region. They agree with the experimental data obtained at $x / \delta_1 = 195$ and are also similar in Cases 1-3. Therefore, only velocity profiles from Case 1 are shown in the figure. The results demonstrate that with respect to the mean velocity, the flow has achieved self-similarity, that is, the velocity profiles are independent of a streamwise location.

The mean velocity profiles in the near field of the splitter plate are shown in Fig. 6. In the figure, experimental results, shown as symbols correspond to the location $x / \delta_1 = 42$, which is the closest to the splitter plate where the measurements were taken. In this region, a different normalization is applied to velocity profiles to demonstrate the wake effect from the splitter plate on the flow velocity. Whereas no sign of the wake effect can be detected in the experimental data, profiles from simulations are affected by the wake at all considered locations in all three cases. In Case 2 though, velocity profiles approach the experimental data faster than in Cases 1 and 3. This indicates that the splitter plate thickness contributes in diminishing the wake from the plate. The effect from the spanwise dimension of the computational domain on the mean flow velocity seems to be minor.

Figure 7 demonstrates the mixing layer growth obtained in simulations. In the figure, the mixing layer thickness (Fig. 7a) and the momentum thickness (Fig. 7b) are shown as functions of the streamwise location. The mixing layer thickness is obtained using Eqs. (12) and (13) as explained earlier in this Section. The momentum thickness is obtained from Eq. (8). Results from simulations are below the experimental values at

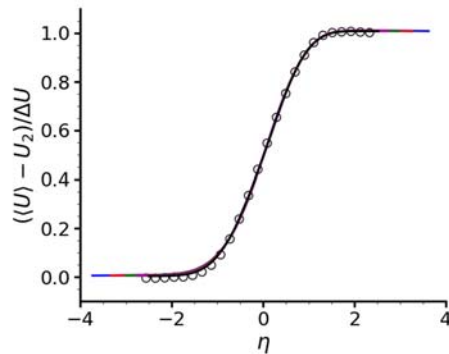


Figure 5. Mean velocity profiles. Notations: solid lines are DNS data, symbols are experimental data⁶ at $x / \delta_1 = 195$. Colors: blue – $x / \delta_1 = 120$, red – $x / \delta_1 = 130$, green – $x / \delta_1 = 140$, magenta – $x / \delta_1 = 150$, black – $x / \delta_1 = 160$.

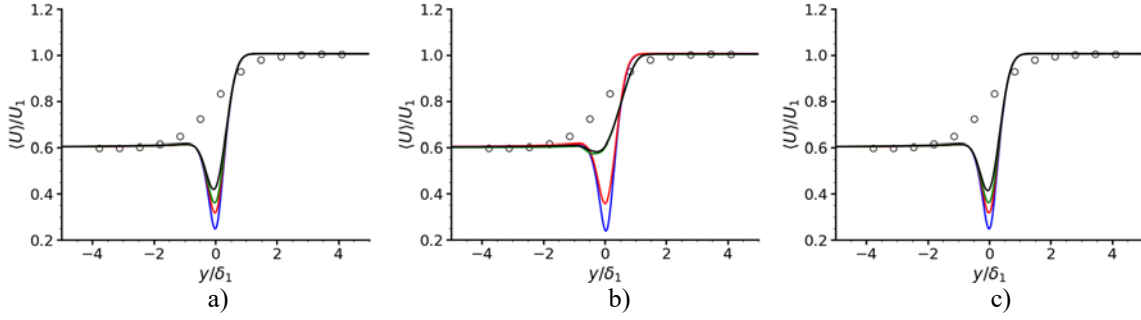


Figure 6. Mean velocity profiles from DNS (solid lines) and experimental data⁶ (symbols) at different streamwise locations, a) Case 1, b) Case 2, c) Case 3. Notations: current DNS results (solid lines), experimental data⁵ taken at $x/\delta_1 = 42$ (symbols). Colors: blue – $x/\delta_1 = 10$, red – $x/\delta_1 = 20$, green – $x/\delta_1 = 30$, black – $x/\delta_1 = 42$.

all flow locations and in all three cases for both parameters. The mixing layer growth rate given by the slope of the curves is close to experimental observations in the three cases, but Case 2 reproduces the flow growth more accurately than the other two cases. The growth of the mixing layer is delayed to compare with the experiments in all cases, but in Case 2, the mixing layer starts to grow much closer to the splitter plate than in Cases 1 and 3.

Results for the momentum thickness show a region where θ remains negative over a section of the domain, which is shorter in Case 2 ($x/\delta_1 < 25$) than in Cases 1 and 3 ($x/\delta_1 < 50$). Negative values of the momentum thickness occur where the wake effect from the splitter plate is significant leading to the mean velocity deficit and the argument of the integral in (8) to be negative, $\langle U \rangle - U_2 < 0$ in this region. This is consistent with the results in Fig. 6 that show the wake effect in the three cases. Further research is required to better understand how to overcome the delay of the mixing layer development observed in the simulations and its possible connection to underdevelopment of the low-speed boundary layer.

Overall, results indicate sensitivity of the mixing layer growth to the plate thickness in simulations, but not as much to the domain dimension in the spanwise direction.

Evolution of the Reynolds stresses normalized by ΔU^2 is shown in Figs. 8-11. In the area close to the splitter plate, simulations from Cases 1 and 3 do not reproduce the Reynolds stresses accurately, with the flow remaining laminar at the locations where experiments show significant presence of turbulence (blue lines in Figs. 8-11a and c). Far downstream in the turbulent flow region ($x/\delta_1 = 143$ and $x/\delta_1 = 160$), profiles of $\langle u^2 \rangle$ and $\langle v^2 \rangle$ overshoot experimental data. The shear stress $\langle uv \rangle$ in Case 1 is similar to the experimental data at these locations, but profiles do not seem to be statistically converged in both cases for the definite conclusions. The Reynolds stress in the spanwise direction is close to the experimental data at $x/\delta_1 = 160$ in Case 3 indicating that increasing the domain dimension in this direction is beneficial for the accurate calculation of this moment.

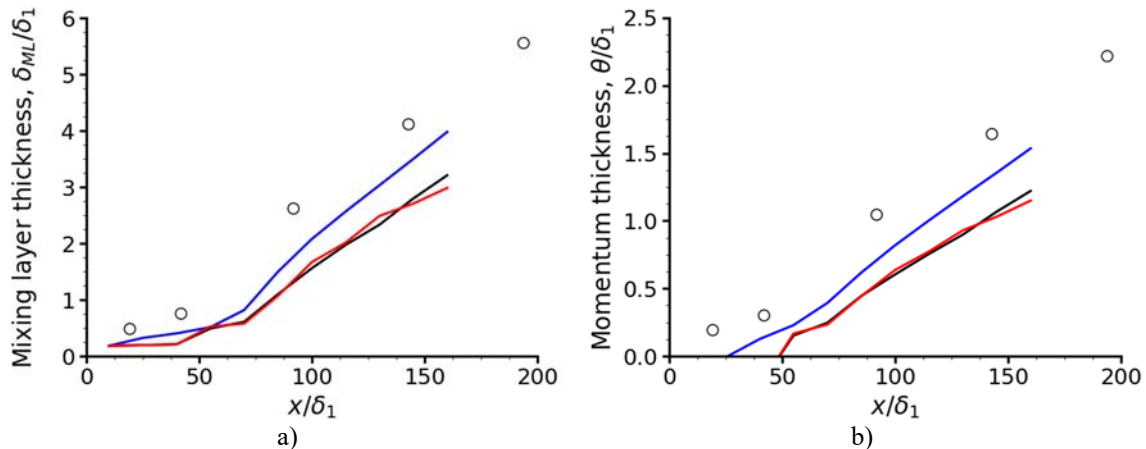


Figure 7. The mixing layer growth: a) mixing layer thickness, b) momentum thickness. Notations: DNS results (solid lines), experimental data⁶ (circles). Colors: black – Case 1, blue – Case 2, red – Case 3.

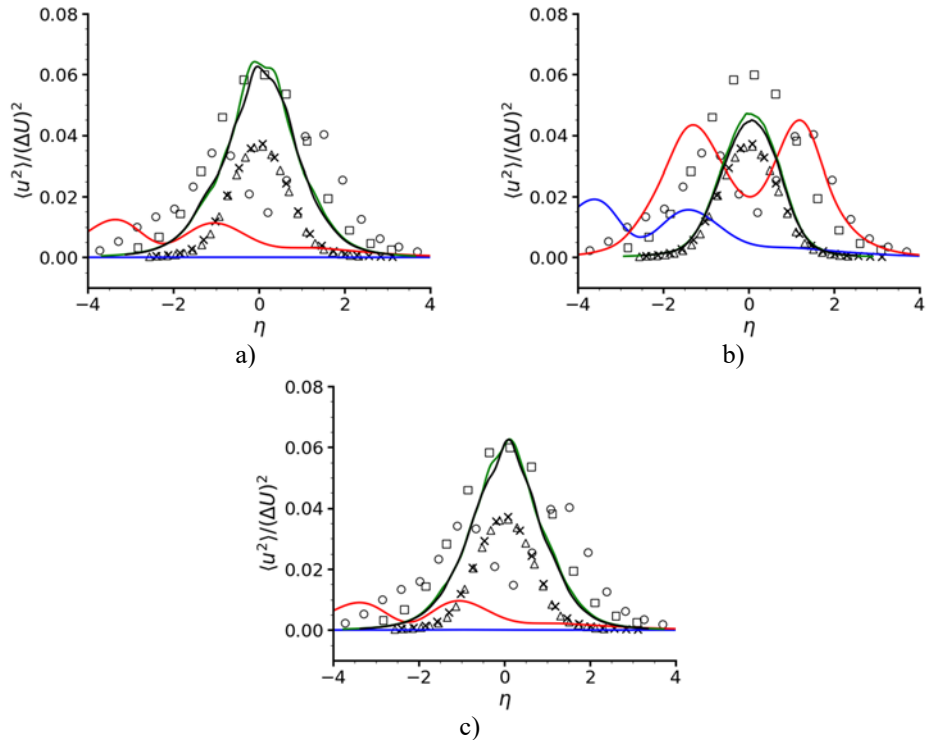


Figure 8. Reynolds stress $\langle u^2 \rangle$ at different streamwise locations: a) Case 1, b) Case 2, c) Case 3. Notations: current DNS results (solid lines), experimental data⁶ (symbols). Colors: blue $-x/\delta_1 = 19.5$, red $-x/\delta_1 = 42$, green $-x/\delta_1 = 143$, black $-x/\delta_1 = 160$. Symbols: circle $-x/\delta_1 = 19.5$, square $-x/\delta_1 = 42$, \times $-x/\delta_1 = 143$, triangle $-x/\delta_1 = 195$.

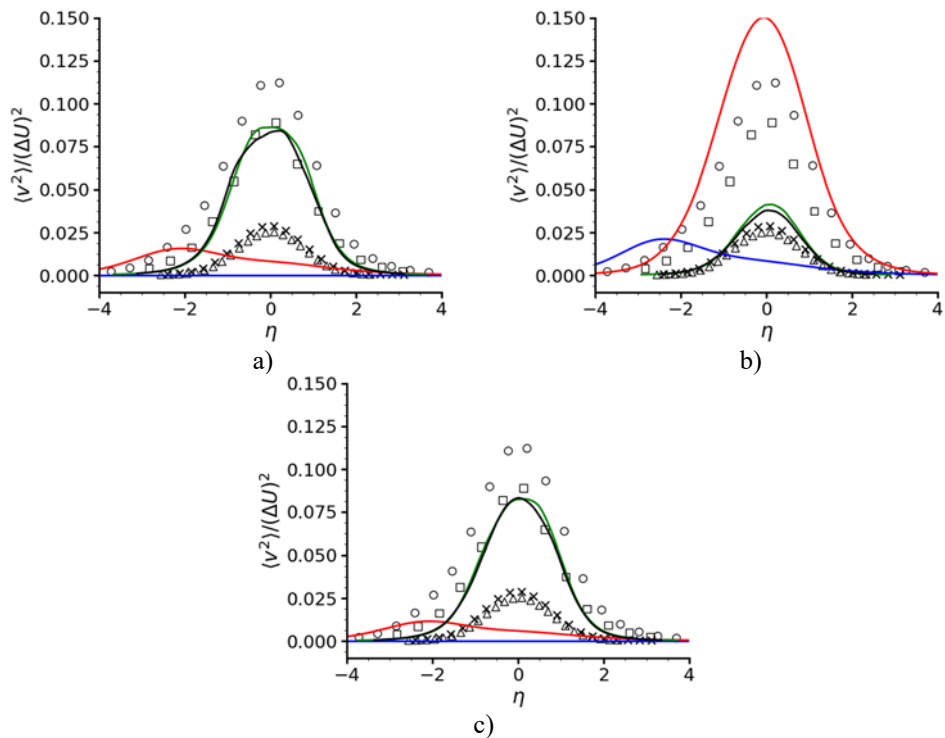


Figure 9. Reynolds stress $\langle v^2 \rangle$ at different streamwise locations, a) Case 1, b) Case 2, c) Case 3. Notations: same as in Fig. 8.

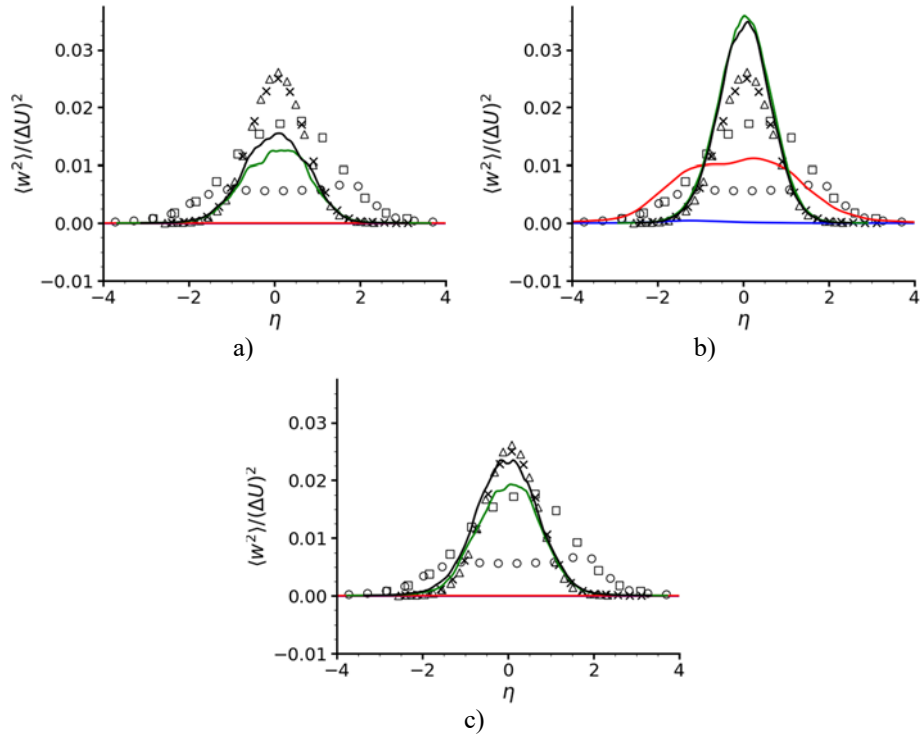


Figure 10. Reynolds stress $\langle w^2 \rangle$ at different streamwise locations, a) Case 1, b) Case 2, c) Case 3. Notations: same as in Fig. 8.

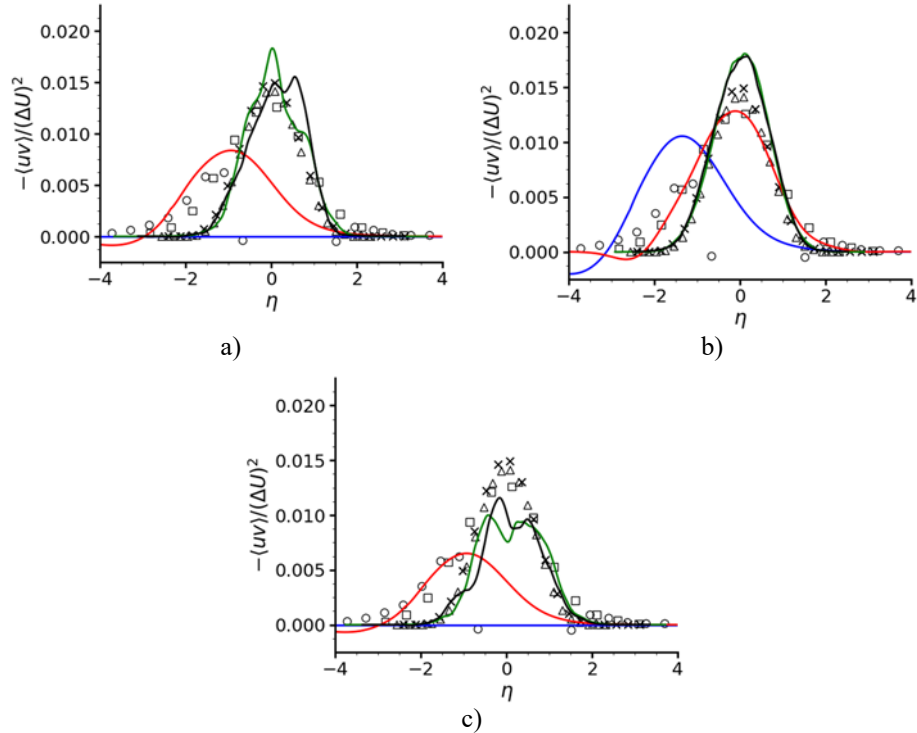


Figure 11. Reynolds stress $\langle uv \rangle$ at different streamwise locations, a) Case 1, b) Case 2, c) Case 3. Notations: same as in Fig. 8.

DNS results for the Reynolds stresses from Case 2 are in an overall better agreement with the experimental data than those from Cases 1 and 3, particularly in the turbulent mixing region. Closer to the mixing layer centerline, DNS data for all Reynolds stresses slightly overshoot in this case those from the experiments, but not as dramatically as in Cases 1 and 3. The data from Case 2 are also more statistically converged than the similar data from the other two cases and show tendency to self-similarity observed in the experiments for these statistics. This is illustrated in more detail in Fig. 12. Self-similarity is not as apparent for $\langle w^2 \rangle$ and $\langle uv \rangle$ in Cases 1 and 3 (Figs. 10a,c and 11a,c).

The results in Figs. 8-12 confirm that the plate thickness is important factor to include in the flow simulations.

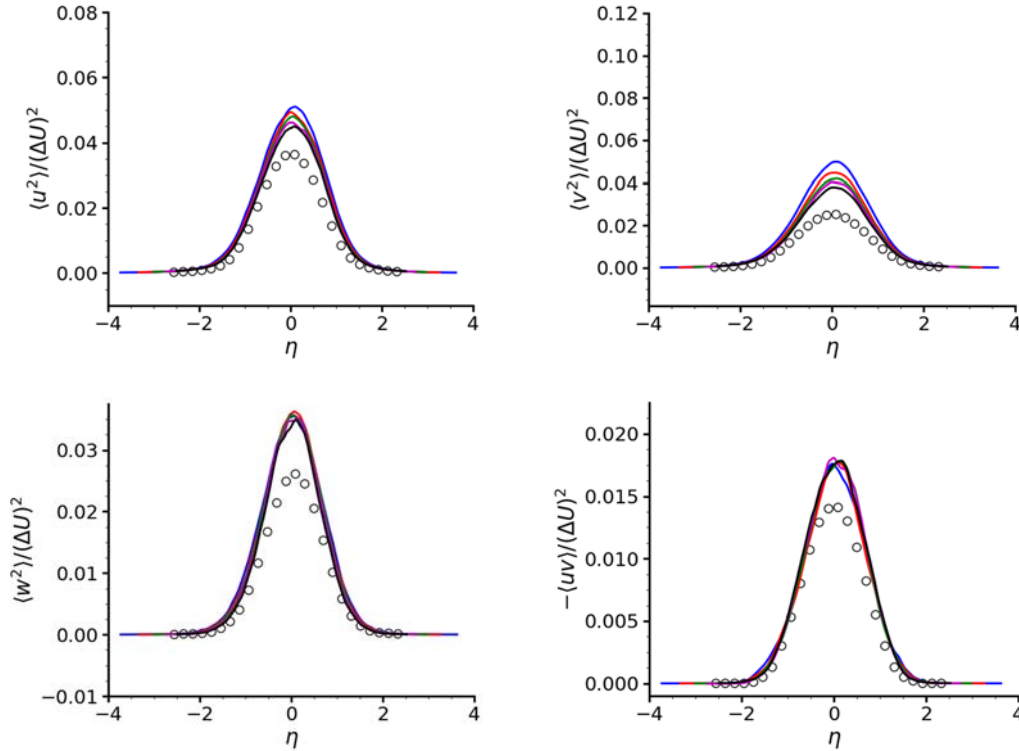


Figure 12. The Reynolds stresses from Case 2 far downstream: Notations: Solid lines – DNS; circles – Experimental data⁶ taken at $x/\delta_1 = 195$. Colors: blue – $-x/\delta_1 = 120$, red – $-x/\delta_1 = 130$, green – $-x/\delta_1 = 140$, magenta – $-x/\delta_1 = 150$, black – $-x/\delta_1 = 160$.

Figure 13 shows the streamwise evolution of the normal Reynolds stresses and the turbulent kinetic energy integrated across the mixing layer. These parameters are determined as follows

$$K(x) = \frac{1}{2\Delta U^2} \int_{-Ly/2}^{Ly/2} \langle u^2 \rangle + \langle v^2 \rangle + \langle w^2 \rangle dy \quad (14)$$

$$K_x(x) = \frac{1}{\Delta U^2} \int_{-Ly/2}^{Ly/2} \langle u^2 \rangle dy \quad (15)$$

$$K_y(x) = \frac{1}{\Delta U^2} \int_{-Ly/2}^{Ly/2} \langle v^2 \rangle dy \quad (16)$$

$$K_z(x) = \frac{1}{\Delta U^2} \int_{-Ly/2}^{Ly/2} \langle w^2 \rangle dy \quad (17)$$

Experimental integral values were approximated by numerical integration of the experimental data using the trapezoidal rule. Results from Cases 1 and 3 confirm the absence of turbulence (in a statistical sense) in these simulations in the area close to the splitter plate at $x/\delta_1 < 42$. Downstream this region, the parameters K_x , K_y , and K start to grow rapidly and overshoot experimental values. The growth of K_z is delayed in both cases until $x/\delta_1 \approx 75$ and does not reach the experimental level within the computational domain. Variations in the domain spanwise

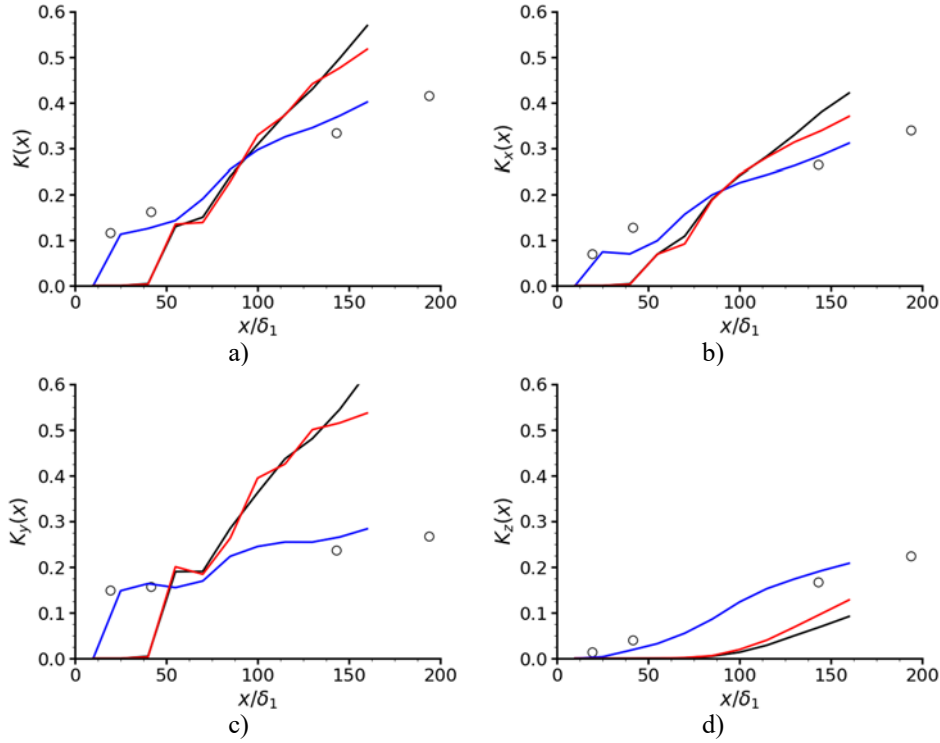


Figure 13. Streamwise evolution of the turbulent kinetic energy integrated across the mixing layer: a) total turbulent kinetic energy (Eq. (14)), b) contribution from streamwise component (Eq. (15)), c), contribution from transverse component (Eq. (16)), and d) contribution from spanwise component (Eq. (17)). Notations: current DNS results (solid lines), experimental data⁶ (circles). Colors: black – Case 1, blue – Case 2, red – Case 3.

dimension have minor effect on the evolution of these flow parameters. The turbulence development in the spanwise direction is suppressed in these cases. On the other hand, the splitter plate thickness has a strong influence on these parameters as seen in Fig. 13 (blue lines). The Case 2 results are in close agreement with the experimental data suggesting that the simulated flow contains the same amount of turbulent kinetic energy as in the experiments with the realistic distribution of this energy in different flow directions.

Snapshots of the turbulent vortex structures in the flow at a simulation time $t \approx 1000$ are shown in Figure 14 for the three cases. Flow visualization was generated using VisIt visualization software³³. The vortices are visualized by iso-surfaces of the Lambda-2 (λ_2) criterion²⁰. According to this criterion, vortices are defined as connected regions where $\lambda_2 \leq 0$. The variable λ_2 is the “second” eigenvalue ($\lambda_1 > \lambda_2 > \lambda_3$) of the tensor $S^2 + \Omega^2$, where $S = \frac{1}{2}[\nabla \mathbf{u} + (\nabla \mathbf{u})^T]$ and $\Omega = \frac{1}{2}[\nabla \mathbf{u} - (\nabla \mathbf{u})^T]$. The purpose of applying a vortex-identification method for flow visualization is not to closely examine the large- and small-scale vortex structures in the flow, which have been a subject of study in numerous experimental³⁻¹⁰ and numerical¹¹⁻¹⁷ works, but to illustrate and compare the mixing layer structure obtained in Cases 1-3.

The flow structure differs significantly in the three cases. In Cases 1 and 3 (Fig. 14a,c), the flow is dominated by large-scale spanwise structures. Potentially turbulent spots can be observed in Case 1 near $x/\delta_1 = 88$ and $x/\delta_1 = 160$. In Case 3, such area occurs near $x/\delta_1 = 160$. Local nature of the observed streamwise vortices and small-scale structures indicates that in these cases, the flow is not fully turbulent, but rather laminar with a presence of “turbulent” spots. Overall, the figure shows benefits of the increased domain dimension in the spanwise direction on the flow development although not as significant as initially expected.

In Case 2 (Fig. 14b), rapid breakdown of large-scale vortices into small-scale structures occurs early in the flow, $40 < x/\delta_1 < 80$, leading to the turbulence development indicated by a presence of small-scale vortices throughout the flow field at $x/\delta_1 > 80$. These results are consistent with conclusions made in Refs. 18 and 19 that the trailing edge of the splitter plate of finite thickness introduces 3D instabilities into the flow that lead to the flow transition to turbulence.

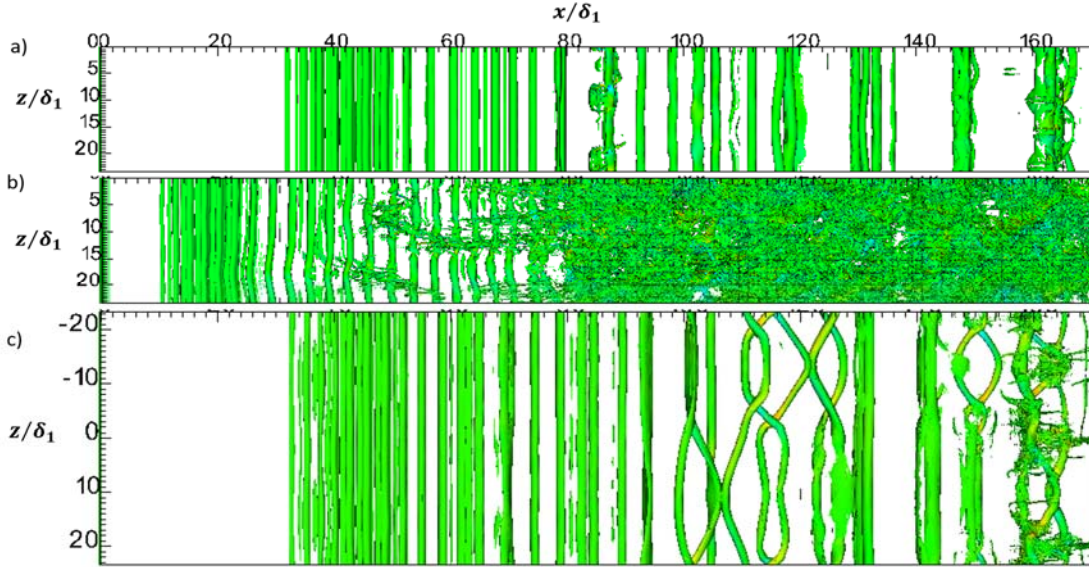


Figure 14. Flow visualization of vortex structures in the mixing layer using iso-surfaces of λ_2 at $\lambda_2 = 0$, colored by instantaneous spanwise velocity, W . Plan view (X-Z plane). a) Case 1, b) Case 2, c) Case 3.

In sum, this study demonstrated that incorporating the splitter plate thickness from experiments into the simulations is a preferable computational strategy compared to an increase in the domain dimension in the spanwise direction. Finite splitter plate thickness leads to an earlier development of turbulence in the mixing layer with the results matching closer to those observed in the experiments. Statistics are also better converged without increasing the computational cost. This strategy is easy to implement and does not rely on the modeled inflow conditions and artificial velocity perturbations. The current results can be further improved by, for example, increasing the development length of the low-speed boundary layer.

V. Conclusions

The current paper presented the results of direct numerical simulation of a spatially developing planar turbulent mixing layer from two co-flowing laminar boundary layers separated by a splitter plate. The goal of the simulations was to explore requirements on the computational domain dimensions that allow for the natural flow development from laminar boundary layers to the turbulent mixing layer within the domain. Simulations were conducted in three flow geometries (Cases 1-3) with the purpose of analyzing particularly the influence of the splitter plate thickness and the spanwise dimension of the computational domain on the mixing layer development. In Case 1, the mixing layer develops downstream the infinitely thin splitter plate. Case 2 corresponds to the flow developing downstream the splitter plate of the finite thickness in the computational domain of the same dimensions as used in Case 1. In Case 3, the domain size in the spanwise direction is doubled to compare with Cases 1 and 2; the splitter plate is the same as in Case 1 (zero thickness).

The study confirmed the conclusion from the previous studies^{18,19} about the importance of incorporating into computations the finite splitter plate thickness for matching the mixing layer growth observed in experiments. The mixing layer thickness growth and the integral values of turbulent kinetic energy across the mixing layer obtained in Case 2 of this study are in close agreement with the experimental data⁶ without any artificial velocity perturbations being seeded into the flow to facilitate turbulence. Dynamics of the Reynolds stresses along the flow streamwise direction is also better reproduced in the Case 2 simulations than in the other two cases.

Increasing the spanwise size of the computational domain (Case 3) allows for the development of spanwise instabilities in the originally planar vortex structures which might be responsible for the correct prediction of the spanwise Reynolds stress in this case. However, this does not facilitate earlier flow transition to turbulence like in Case 2, and the disagreement with the experimental data for other quantities is still severe. More detailed study of this effect would be of further interest, but currently is too costly.

Thus, both computational strategies – incorporating the finite splitter plate thickness in simulations and increasing the domain spanwise dimension – contribute in improving the accuracy of the simulation results, with the former being of primary significance for earlier flow transition to turbulence. The turbulent mixing layer has been achieved in the

current study. However, to achieve the mixing layer self-similarity at locations observed in experiments, further investigation of the simulation parameters is required.

Acknowledgments

We would like to acknowledge the computational time allocation on Pleiades supercomputer at NASA's High-End Computing Capability, where the simulations were conducted, as well as the Center for Advanced Research Computing, University of New Mexico, where a part of the simulations and post-processing was conducted.

References

- ¹Weller, H. G., Tabor, G., Gosman, A. D., Fureby, C., "Application of a Flame-Wrinkling LES Combustion Model to a Turbulent Mixing Layer," *Symposium (Intl.) on Combustion*, Vol. 27, No. 1, 1998, pp. 899-907.
- ²Yoder, D., Debones, J., and Georgiadis, N., "Modeling of Turbulent Free Shear Flows," *Computers & Fluids*, Vol. 117, 2015, pp. 212-232.
- ³Browand, F., and Latigo, B., "Growth of the Two Dimensional Mixing Layer from a Turbulent and Nonturbulent Boundary Layer," *Physics of Fluids*, Vol. 22, No. 6, 1979, pp. 1011.
- ⁴Dimotakis, P. E., and Brown, G. L., "The Mixing Layer at High Reynolds Number: Large-Structure Dynamics and Entrainment", *Journal of Fluid Mechanics*, Vol. 78, No. 3, 1976, pp. 535.
- ⁵Huang, L.S., and Ho, C.M., "Small scale transition in a plane mixing layer," *Journal of Fluid Mechanics*, Vol. 210, 1990, pp. 475-500.
- ⁶Bell, J. H., and Mehta, R. D., "Development of a two-stream mixing layer from tripped and untripped boundary layers," *AIAA Journal*, Vol. 28, No. 12, 1990, pp. 2034-2042.
- ⁷Dziomba, B., and Fiedler, H. E., "Effects of Initial Conditions on Two-Dimensional Free Shear Layers," *Journal of Fluid Mechanics*, Vol. 152, March 1985, pp. 419-442.
- ⁸Mehta, R. D., and Westphal, R. V., "Near-Field Turbulence Properties of Single- and Two-Stream Plane Mixing Layers," *Experiments in Fluids*, Vol. 4, Sept. 1986, pp. 257-266.
- ⁹Mehta, R. D., and Westphal, R. V., "Effect of Velocity Ratio on Plane Mixing Layer Development," *Proceedings of the Seventh Symposium on Turbulent Shear Flows*, Stanford Univ., Stanford, CA, Aug. 21-23, 1989, pp. 3.2.1-3.2.6.
- ¹⁰Patel, R. P., "Effects of Stream Turbulence on Free Shear Flows," *Aeronautical Quarterly*, Vol. 29, Feb. 1978, pp. 33-43
- ¹¹Balaras, E., Piomelli, U., and Wallace, J. M., "Self-similar states in turbulent mixing layers", *Journal of Fluid Mechanics*, Vol. 446, No. 2001, 2001, pp. 1-24.
- ¹²Rogers, M. M., and Moser, R. D., "The Three-Dimensional Evolution of a Plane Mixing Layer: the Kelvin-Helmholtz Rollup," *Journal of Fluid Mechanics*, Vol. 243, 1992, pp. 183-226.
- ¹³Rogers, M. M., and Moser, R. D., "Direct simulation of a self-similar turbulent mixing layer," *Phys. Fluids*, Vol. 6, No. 2 1994, pp. 903.
- ¹⁴Wang, Y., Tanahashi, M., and Miyauchi, T., "Coherent fine scale eddies in turbulence transition of spatially-developing mixing layer," *Intl. Journal of Heat and Fluid Flow*, Vol. 28, 2007, pp. 1280-1290.
- ¹⁵Attili, A., and Bisetti, F., "Statistics and scaling of turbulence in a spatially developing mixing layer at $Re_\lambda = 250$," *Phys. Fluids*, Vol. 24, No. 3, 2012, 035109.
- ¹⁶McMullan, W. A., "Spanwise Domain Effects on the Evolution of the Plane Turbulent Mixing Layer," *International Journal of Computational Fluid Dynamics*, Vol 29, Nos. 6-8, 2015, pp. 333-345.
- ¹⁷McMullan, W. A., and Garrett, S. J., "Initial Condition Effects on Large Scale Structure in Numerical Simulations of Plane Mixing Layers," *Physics of Fluids*, Vol. 28, No. 1, 2016, 15111.
- ¹⁸Laizet, S., and Lamballais, E., "Direct numerical simulation of a spatially evolving flow from an asymmetric wake to a mixing layer," *Direct and Large-Eddy Simulation VI*. Springer Netherlands, 2006. 467-474.
- ¹⁹Laizet, S., Lardeau, S., and Lamballais, E., "Direct numerical simulation of a mixing layer downstream a thick splitter plate." *Physics of Fluids*, Vol. 22, No. 1 pp. 015104, 2010.
- ²⁰Jeong, J, and Hussain, F., "On the Identification of a Vortex," *Journal of Fluid Mechanics*, Vol. 285, 1995, pp. 69-94.
- ²¹A. T. Patera, "A spectral element method for fluid dynamics: laminar flow in a channel expansion," *Journal of Computational Physics*, Vol. 54, 1984, pp. 468-488.
- ²²Fischer, P., Kruse, J., Mullen, J., Tufo, H., Lottes, J. & Kerkemeier, S., "NEK5000: Open source spectral element CFD solver," 2008. URL: <https://nek5000.mcs.anl.gov/index.php/MainPage>.
- ²³Deville, M. O.; Fischer, P. F.; Mund, E. H. *High-Order Methods for Incompressible Fluid Flow*; Cambridge Monographs on Applied and Computational Mathematics, 9; Cambridge University Press: Cambridge, UK, 2002.
- ²⁴Tomboulides, A., Lee, J., and Orszag, S., "Numerical simulation of low Mach number reactive flows," *J. Scientific Computing*, Vol. 12, No. 2, 1997, pp. 139-167.
- ²⁵Karniadakis, G., Israeli, M., and Orszag, S., "High-order splitting methods for the incompressible Navier-stokes equations," *J. Comput. Phys*, Vol. 97, No. 2, 1991, pp. 414-443.
- ²⁶Dimotakis, P. E., "The mixing transition in turbulent flows," *J. Fluid Mech.*, Vol. 409, No. 4, 2000, pp. 69-98.
- ²⁷Ohlsson, J., Schlatter, P., Fischer, P. F., and Henningson, D. S., "Direct numerical simulation of separated flow in a three-dimensional diffuser," *J. Fluid Mech.*, Vol. 650, 2010, pp. 307.

²⁸Vinuesa, R., Hosseini, S. M., Hanifi, A., Henningson, D. S., and Schlatter, P., “Direct numerical simulation of the flow around a wing section using high-order parallel spectral methods,” *Intl. Symp. on Turbulence and Shear Flow Phenomena*, January, 2015, pp. 1-6.

²⁹Orszag, S. A., Israeli, M., & Deville, M. O., “Boundary conditions for incompressible flows,” *J. Scientific Computing*, Vol. 1, No. 1, 1986, pp. 75-111.

³⁰The Scipy Community, “Scipy.optimize.curve_fit,” Open-source library for Python programming language. URL: https://docs.scipy.org/doc/scipy/reference/generated/scipy.optimize.curve_fit.html [cited 17 April 2017].

³¹Schetz, J.A. and Bowersox, R. D. W., *Boundary Layer Analysis*, 2nd ed., AIAA Education Series, AIAA, Virginia, 2011, pp. 99-103.

³²Slessor, M. D., Bond, C. L., and Dimotakis, P. E., “Turbulent Shear-Layer Mixing at High Reynolds Numbers: Effects of Inflow Conditions”, *Journal of Fluid Mechanics*, Vol. 376, 1998, pp. 115–138.

³³Childs, H., Bruger, E. et al., “VisIt: An End-User Tool For Visualizing and Analyzing Very Large Data”, *High Performance Visualization--Enabling Extreme-Scale Scientific Insight*, CRC Press, 2012, pp. 357-372.